JOURNAL OF GEOPHYSICAL RESEARCH, VOL. 115, C06004, doi:10.1029/2009JC006054, 2010

Relationship between ocean velocity and motionally induced electrical signals: 2. In the presence of sloping topography

Zoltan B. Szuts[1,2]

Received 14 December 2009; accepted 8 January 2010; published 5 June 2010.

[1] Motionally induced electric fields and electric currents in the ocean depend to first order solely on the vertical dimension. We investigate the significance of two-dimensional (2-D) perturbations that arise in the presence of sloping topography. The full electric response is calculated for a schematic geometry that contains a topographic slope, has a two-layer ocean with a layer of sediment beneath, and is described by five nondimensional parameters. When considered over the realistic ranges of topographic aspect ratio (the ratio of mean water depth to topographic width), topographic relief, sediment thickness, and sediment conductivity, velocity errors arising from 2-D perturbations are found to be less than a few percent of the dominant one-dimensional (1-D) signal. All errors depend on the topographic aspect ratio to the power of 1.9 and have linear dependence on topographic relief and the depth of the surface jet. Depth-uniform velocity errors are roughly proportional to the 1-D sediment conductance ratio, whereas depth-varying velocity errors are independent of sediment thickness or conductivity. Two-dimensional perturbations decay with a half width of 0.2–1 times the 1-D effective water depth. The magnitude of estimated errors is consistent with those found at a measurement location with strong 2-D perturbations. This study extends the first-order theory to the maximum expected aspect ratios for topography and finds small perturbations with simple dependencies. Overall, the 1-D approximation is found to be adequate for interpreting observations at all but the most extreme locations.

Citation: Szuts, Z. B. (2010), Relationship between ocean velocity and motionally induced electrical signals: 2. In the presence of sloping topographic, *J. Geophys. Res.*, *115*, C06004, doi:10.1029/2009JC006054.

1. Introduction

[2] Measuring horizontal electromagnetic fields (EM) that are generated by the motion of seawater through the Earth's magnetic field is a convenient way to indirectly measure ocean velocity. High quality observations have been made from a variety of platforms (including submarine cables, bottom-mounted sensors, vertical profilers, and horizontally drifting floats) and the availability of commercial EM instruments and cables indicate a wide accessibility to the oceanographic community.

[3] The technique has unique advantages, and in many cases EM observations are the only practical means for measuring the desired quantity. Profiling floats measure high vertical resolution profiles of velocity and can be used for either ship-based or autonomous deployments. Stationary sensors such as bottom electrometers or submarine cables measure a quantity dynamically similar to volume transport [*Luther and Chave*, 1993], the utility of which is exemplified by monitoring of the meridional overturning circulation in the North Atlantic [*Cunningham et al.*, 2007]. The increasing availability of motional induction techniques, however, necessitates a closer inspection of the underlying theory in a broader range of environments than considered in the literature.

[4] The theory of motional induction that relates ocean velocity to electric fields (EF) and electric currents depends only on the vertical dimension, a one-dimensional (1-D) relationship. This is the form typically used to interpret observations and to calculate water velocity.

[5] The higher-order terms of this theory that depend on velocity or topographic gradients have not yet been directly calculated or observed in situations where they are expected to be significant. Although small horizontal perturbations of velocity and topography were considered by *Sanford* [1971], his use of a perturbation technique means that the solution is strictly valid only for small gradients and cannot be directly applied to regions such as continental slopes or at edges of highly energetic eddies.

[6] Here we are concerned with the structure and magnitude of oceanic electric fields in the presence of topographic slopes. Electromagnetic solutions are calculated directly for

[1]Applied Physics Laboratory and School of Oceanography, University of Washington, Seattle, Washington, USA.
[2]Now at Max-Planck-Institut für Meterologie, Hamburg, Germany.

0148-0227/10/2009JC006054

a simplified geometry containing topographic slopes, and the solutions are then evaluated for the magnitude of perturbation from the first-order theory. In particular, we focus on the errors that arise in calculating velocity from electric field observations in the presence of these higher-order effects. A companion article [*Szuts*, 2010, hereafter SzI] considers the role of horizontal velocity gradients in generating higher-order EM perturbations. A complementary paper (Z. B. Szuts, in preparation, 2010, hereafter Sz10) analyzes electric field observations collected across the Gulf Stream at Cape Hatteras, North Carolina, USA and considers the same processes discussed here but for observations in a specific and complex location.

[7] The theory of motional induction and the physical basis for higher order terms is presented first in section 2, after which our method of evaluating the 2-D perturbations is presented in section 3. Given that the theory and the method of analysis are very similar to that of SzI, only the essential features are reiterated here. The electromagnetic solutions are described next (section 4). A discussion of these results follows (section 5), including a synthesis with the results of SzI, and we conclude with section 6.

2. Theory

[8] Electric fields occur in the ocean due to the motion of conductive salt water through the Earth's magnetic field; this is generally called motional induction. The thin aspect ratio of the ocean and the assumption of small horizontal gradients of velocity and topography allow for great simplification of the three-dimensional (3-D) governing equations. Although other analyses focus on additional details of oceanic electromagnetism, the results of *Sanford* [1971] are most appropriate for this investigation because his perturbation technique includes the effect of small horizontal gradients. Other theoretical analyses offer discussions of long period waves [*Larsen*, 1968, 1971; *Tyler*, 2005], the influence of deep earth conductivity structure [*Chave and Luther*, 1990], and spherical coordinates [*Tyler and Mysak*, 1995b] among others.

[9] The principal electric fields ($\boldsymbol{E}$) and electric currents ($\boldsymbol{J}$) generated by ocean flow fall into two modes. The traditional and generally more important mode restricts $\boldsymbol{E}$ and $\boldsymbol{J}$ to the vertical plane. This is a toroidal mode that describes, for instance, electric currents in the surface layer forced by surface flow with weaker electric currents returning in the motionless deep ocean. The magnitude of $\boldsymbol{E}$ or $\boldsymbol{J}$ depends on the strength of the vertically averaged (defined as barotropic) or vertically varying (defined as baroclinic) velocity signals, respectively. At the simplest, this is exemplified by two cases of an ocean over a nonconductive seafloor: if water motion is vertically uniform, $\boldsymbol{E}$ is maximal and $\boldsymbol{J}$ is zero everywhere, in analogy to the Hall effect of classical physics; while if water motion is purely baroclinic there is no $\boldsymbol{E}$ but $\boldsymbol{J}$ is maximal.

[10] The second mode, called poloidal, is characterized by $\boldsymbol{E}$ that uniformly fill the water column and are directed in the horizontal plane. This mode only exists in situations where there are gradients in the downstream direction and thus is a 3-D effect. Such effects, often called nonlocal currents, will not be discussed further [*Tyler et al.*, 2003].

[11] The dominant solution found by *Sanford* [1971] is now well established [*Chave and Luther*, 1990; *Tyler and Mysak*, 1995a]. The analytical form of his solutions, though dependent on initial assumptions, remains instructive as it hints at the underlying physical factors relating the EM solution to perturbations of velocity and topography. Among his assumptions are: a horizontal ocean bottom (H) with small topographic perturbations (h, where $h/H \ll 1$), width scales (L) much larger than bottom depth ($H/L \ll 1$), predominantly horizontal oceanic velocity ($\boldsymbol{v} = (u, v, 0)$), distant lateral boundaries, a layer of underlying sediment that has a uniform electrical conductivity, and a highly conductive deep earth to approximate the deep but conductive mantle.

[12] Although it is readily shown that time variations of motionally induced $\boldsymbol{E}$ in turn induce magnetic fields that are negligible compared to the Earth's magnetic field, a less evident process is inductive coupling between the ocean and the conductive mantle. By considering the frequency and spatial extent of nontidal oceanic flow, which are generally low frequency (periods larger than a day) and smaller than basin scale (<1000 km), the use of a quasi-static form for motional induction is accurate to less than 5% [*Sanford*, 1971; *Chave and Luther*, 1990].

[13] In general form, the quasi-static horizontal electric field $\boldsymbol{E}_h$ is

$$-\boldsymbol{E}_h = \nabla_h \phi = \boldsymbol{v} \times \hat{\boldsymbol{k}} F_z - \boldsymbol{J}_h/\sigma, \tag{1}$$

where ∇_h is the horizontal gradient operator, ϕ is electric potential, $\boldsymbol{v}$ is oceanic velocity, F_z is the vertical component of Earth's magnetic field, $\hat{\boldsymbol{k}}$ is the vertical unit vector (pointing upward), σ is electrical conductivity, and $\boldsymbol{J}_h$ is horizontal electric current density. The electromotive driving force $\boldsymbol{v} \times \hat{\boldsymbol{k}} F_z$ is what generates electric field and electric currents.

[14] A general form for horizontal electric current density divided by conductivity with the above assumptions is [*Sanford*, 1971]

$$\frac{\boldsymbol{J}_h}{\sigma} = (\boldsymbol{v} - \bar{\boldsymbol{v}}^*) \times F_z \hat{\boldsymbol{k}} - \nabla_h \left\{ \frac{1}{H(1+\lambda)} \int_{-H}^{\zeta} \hat{\boldsymbol{k}} \cdot (\boldsymbol{v} \times \boldsymbol{F}) z' \, dz' + \int_{-H}^{z} \hat{\boldsymbol{k}} \cdot (\boldsymbol{v} \times \boldsymbol{F}) \, dz' \right\}, \tag{2}$$

with

$$r = \sqrt{(x-x')^2 + (y-y')^2}$$
$$D = H + \zeta - h + \frac{\sigma_s}{\sigma}(H_s - H + h) \tag{3}$$
$$\bar{\boldsymbol{v}}^* = \int_{-H+h}^{\zeta} \sigma \boldsymbol{v} \, dz' \Big/ \int_{-H_s}^{\zeta} \sigma \, dz',$$

where ζ is the sea surface, $-H$ is the mean position of the seafloor, h is the perturbation of the seafloor, $-H_s$ is the bottom of conductive sediment, D is a scaled water depth, σ_s is the uniform sediment conductivity, λ is the sediment conductance factor ($D/H = 1 + \lambda$), and $\bar{\boldsymbol{v}}^*$ is the conductivity-weighted vertically averaged velocity. The coordinate

directions are as follows: x is positive east, y is positive north, and z is positive upward. The first and second terms on the right-hand side of (2) represent first-order and higher-order processes. The addition of a third term caused by 3-D effects makes $\boldsymbol{J}_h$ nondivergent to order H^2/L^2 [*Sanford*, 1971].

2.1. First-Order Term

[15] The first term on the right-hand side of (2) is the principal toroidal mode. This term is one-dimensional because it only depends on the vertical dimension: a vertical integral of velocity (3) defines the depth-uniform electric field $\overline{\boldsymbol{v}}^* F_z$, while vertical variations of $\sigma(\boldsymbol{v}(z) - \overline{\boldsymbol{v}}^*)$ determine the electric current density. The 1-D approximation used to interpret observations is obtained by keeping only this term, which is interchangeably called 1-D or first order.

[16] The quantity $\overline{\boldsymbol{v}}^*$ corresponds physically to the vertically uniform horizontal electric field divided by F_z and is called the vertically averaged conductivity-weighted velocity. In the 1-D approximation, the constraint that $\boldsymbol{J}_h$ must vertically integrate to zero to conserve charge leads to the definition of $\overline{\boldsymbol{v}}^*$.

[17] The electric current density divided by σ is the difference between that driven by the depth-uniform electric field and that generated by local horizontal water motion, $(\boldsymbol{v}(z) - \overline{\boldsymbol{v}}^*) \times \hat{\boldsymbol{k}} F_z$. In the limiting situation where the flow field is entirely barotropic and there is no sediment layer, there will be no electric currents.

[18] A simpler definition of $\overline{\boldsymbol{v}}^*$ is obtained by simplifying the numerator and denominator of (3). A Reynolds decomposition of the numerator defines the vertical correlation factor γ

$$\frac{1}{H - h + \zeta} \int_{-H+h}^{\zeta} \sigma \boldsymbol{v} \, dz = \overline{\sigma \boldsymbol{v}} = \overline{\sigma}\,\overline{\boldsymbol{v}} + \overline{\sigma' \boldsymbol{v}'} = \overline{\sigma}\,\overline{\boldsymbol{v}}(1 + \gamma), \quad (4)$$

where for the variables $\boldsymbol{v}(z)$ and $\sigma(z)$, $\overline{\boldsymbol{v}}$ and $\overline{\sigma}$ indicate a vertical average in the water column and $\boldsymbol{v}'$ and σ' indicate perturbations about the vertical mean.

[19] Dividing the denominator by the vertical conductance of the water column and rearranging gives

$$\begin{aligned} 1 + \lambda &= \int_{-H_s}^{\zeta} \sigma(z) \, dz \Big/ \int_{-H+h}^{\zeta} \sigma(z) \, dz \\ &= 1 + (H_s - H + h)\sigma_s / (H - h + \zeta)\overline{\sigma}, \end{aligned} \quad (5)$$

where λ is the bottom conductance factor, the ratio of the sediment conductance to the water column conductance.

[20] Combining (4) and (5) yields a simplified form of $\overline{\boldsymbol{v}}^*$ more suitable for interpreting observed $\boldsymbol{E}$

$$\overline{\boldsymbol{v}}^* = \overline{\boldsymbol{v}}\left(\frac{1 + \gamma}{1 + \lambda}\right). \quad (6)$$

Although this form has no horizontal dependence because of the assumption of $H/L \ll 1$, *Chave and Luther* [1990] show that the variables $\overline{\boldsymbol{v}}^*$, γ, and λ are horizontally averaged within a few times the water depth.

[21] The factor λ quantifies the amount of shorting through the bottom sediment. It is closely related to the equivalent bottom depth D (defined in (3), or alternatively $D = H\,(1 + \lambda)$), which is the depth of the water column plus a thickness of seawater with the same conductance as the sediments. Thus, the barotropic velocity generates an electric field that is reduced by the additional conductance of the seafloor. The electric field is the quantity that is measured by stationary sensors such as seafloor electrometers or submarine cables [see SzI].

[22] The vertical correlation factor $\gamma = \overline{\sigma' \boldsymbol{v}'} / \overline{\sigma \boldsymbol{v}}$ corrects for correlations of velocity and water conductivity that alter the electric field $\overline{\boldsymbol{v}}^* F_z$. For instance, if a layer of fast moving water (large motional induction source) is also more conductive, then that layer drives a larger electric current at that depth compared to a uniformly conductive case. The larger electric current in turn generates a larger electric field. The sign of γ is positive in this case, and $\overline{\boldsymbol{v}}^*$ is accordingly larger. Measurements of temperature and salinity simultaneous with $\boldsymbol{J}_h/\sigma$ allow direct calculation of γ, and prior calculations of γ found it to have less than a 10% influence on $\overline{\boldsymbol{v}}^*$ for open ocean baroclinic modes [*Chave and Luther*, 1990; *Szuts*, 2004]. The quantity $\boldsymbol{J}_h/\sigma$ is sensed by vertical profiling floats (e.g., XCP or EM-APEX), because they drift horizontally at the local water velocity and so only sense the potential across their skin generated by $\boldsymbol{J}_h$ [see SzI].

2.2. Higher-Order Term: Horizontal Gradients

[23] The second term on the right-hand side of (2) is a higher-order term because it scales as H/L. It is also two-dimensional (toroidal) because it couples with a term of similar form for J_z (not shown). The poloidal mode (not shown) also scales as H/L but describes 3-D effects.

[24] The second term is nonzero if there are horizontal gradients of H, λ, $\boldsymbol{F}$ or velocity. It includes both depth-uniform and depth-varying components (the first and second integrals of term 2, respectively). In analogy with the horizontal averaging of the first-order term, it is expected that the higher order terms depends on a region within a few times the water depth. The H/L scaling explains why the 1-D approximation is sufficiently accurate for the small aspect ratios found in the open ocean.

[25] In highly energetic regions that are often of interest to physical oceanographers, however, h/H is not necessarily $\ll 1$. The perturbation technique used to obtain (2) is not valid for situations that break the initial assumptions, and thus to accurately calculate the EM response under such conditions it is necessary to calculate solutions with alternative techniques.

3. Approach for Resolving Higher-Order Electric Fields

[26] Because of the difficulty of obtaining general analytical forms for arbitrarily large gradients of topography, we instead consider a schematic geometry that contain gradients in a two-dimensional plane. Quantifying the two-dimensional (2-D) perturbations is not straightforward, and so the analysis methods used must also be specified.

3.1. Schematic Geometry

[27] The geometry considered has three layers (Figure 1): a surface ocean layer moving in slab motion, a motionless deep ocean with variable thickness because of topography, and a uniformly thick and mildly conductive sediment layer at the bottom. It is fully described by seven parameters: the

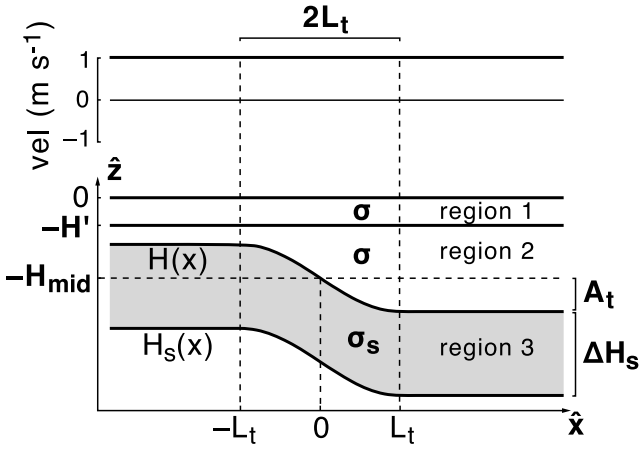

Figure 1. Schematic geometry for which magnetostatic solutions are calculated. (bottom) There are three layers: a surface ocean jet in slab motion (region 1), a motionless deep ocean that contains the changing water depth (region 2), and a layer of conductive sediment (region 3). (top) The surface layer moves into the page (positive $\hat{\boldsymbol{y}}$) with uniform velocity. The seven parameters that define the geometry are shown in bold.

half width of the slope L_t, the topographic relief 2 A_t, the depth of the surface layer H', the water depth at the center of the slope H_{mid}, the sediment thickness ΔH_s (= $H_s(x) - H(x)$), the electrical conductivity of the water σ, and the conductivity of the sediment σ_r. The bottom depth $H(x)$ is chosen of the form

$$H(x) = \begin{cases} -H_{\mathrm{mid}} - A_t & x < -L_t \\ -H_{\mathrm{mid}} + A_t \sin\left(\dfrac{\pi x}{2L_t}\right) & -L_t \le x \le L_t \\ -H_{\mathrm{mid}} + A_t & L_t < x \end{cases}, \qquad (7)$$

because it provides a continuous seafloor that has uniform water depth on either side of the topographic slope.

[28] These seven parameters can be reduced to five nondimensional ones: the depth H_{mid} is used to make four from the remaining length scales, L_t, A_t, ΔH_s, and H', while the fifth is the relative sediment conductivity $\sigma_r = \sigma_s/\sigma$. Note that the jet depth and the topographic relief limit each other, such that $0 < H' < H_{\mathrm{mid}} - A_t$. These nondimensional parameters are varied systematically to obtain solutions over the multidimensional parameter spaces.

[29] Although the results are analyzed based on the nondimensionalized parameters, the solutions are calculated with realistic values for each parameter. The uniform velocity v_0 of the surface layer is set at 1 m s^{-1}, an appropriate value for energetic flows in the ocean. The equations are linear with respect to v_0, so this choice is without loss of generality. The Earth's magnetic field is set to be representative of midlatitude northern hemisphere values: F_z = −40,000 nT. The horizontal magnetic field is not considered, because no physically relevant signals are generated by it for a velocity field of infinite extent.

[30] Implicitly assumed by the three-layer geometry is a nonconductive crust underlying the sediment layer. Realistically, the crust has conductivities of 0.0001–0.03 S m^{-1} [*Chave et al.*, 1992; *Simpson and Bahr*, 2005], which is at least an order of magnitude smaller than typical sediment conductivity and does not support a significant flow of electric current for the motionally induced signals considered here.

3.2. Calculating Two-Dimensional Perturbations

[31] The two-dimensional solutions can be considered as the sum of the expected signal from the first-order solution plus a 2-D perturbation: the depth-uniform signal is contained in $\boldsymbol{E}$, while the depth-varying signal is contained in $\boldsymbol{J}/\sigma$. The magnitude of the perturbation is the primary focus, but its shape is also considered by the decay half width of the perturbations.

3.2.1. Depth-Uniform Mode

[32] The depth-uniform mode is the vertically uniform electric field ($\overline{\boldsymbol{v}}^* F_z$) defined in (6). In the 1-D approximation it is driven by the vertically averaged velocity ($\overline{\boldsymbol{v}}$) with proportionality factors due to sediment conductance (λ) and vertical correlations of conductivity and velocity (γ, 0 by definition).

[33] For 2-D situations E_x is no longer vertically uniform, so a 2-D quantity $\overline{\boldsymbol{v}}^*_{2\text{-D}}$ is calculated by averaging E_x in the water column and dividing by F_z. Because the conductivity of the sediment is by necessity fully specified for our modeling approach, unlike when making measurements in the ocean, the shorting of conductive bottom sediment is corrected by multiplying by the 1-D quantity $1 + \lambda_{1\text{-D}}$. The depth-uniform perturbation (in m s^{-1}) is then defined as

$$\overline{\delta}(x) = \overline{\boldsymbol{v}}(x) - \overline{\boldsymbol{v}}^*_{2\text{-D}}(x)\,(1 + \lambda_{1\text{-D}}). \qquad (8)$$

To obtain one number that characterizes the magnitude of the depth-uniform error for a given set of parameters, we define a depth-uniform error ϵ by calculating the standard deviation of $\overline{\delta}$ over the region $|x| < L_t$. Relative errors are found by dividing by $\overline{\boldsymbol{v}}$, or $\boldsymbol{v}H'/H$.

3.2.2. Depth-Varying Mode

[34] The depth-varying perturbation is the difference between $\boldsymbol{J}/\sigma$ predicted by the 1-D approximation and the 2-D value. Cast into units of velocity, the 2-D perturbation is

$$\delta'(x,z) = v(x,z) - \frac{J_x(x,z)}{\sigma(z)F_z} - \overline{\delta}'(x). \qquad (9)$$

A vertical mean $\overline{\delta'}$ is subtracted to remove the influence of the depth-uniform mode

$$\overline{\delta}'(x) = \frac{1}{H(x)} \int_{-H(x)}^{0} \left[v(x,z) - \frac{J_x(x,z)}{\sigma F_z} \right] \mathrm{d}z, \qquad (10)$$

where H is explicitly shown to vary with x. Relative perturbations are obtained by scaling with the maximum velocity v_0 = 1 m s^{-1}.

[35] The vertical dimension of δ' is compressed by taking the vertical second moment δ'_{std}

$$\delta'_{\mathrm{std}}(x) = \left(\frac{1}{H} \int_{-H}^{0} \delta'^2 \,\mathrm{d}z \right)^{1/2}. \qquad (11)$$

The magnitude of depth-varying perturbations is characterized by definition of a depth-varying error ϵ', calculated by the second moment of δ'_{std} over $|x| < L_t$.

[36] In practice, the correction to absolute velocity $\overline{\delta'}$ is usually calculated from reference velocities collected over less than the full water column, adding a potential bias to the depth-varying velocity error. The second moment and maximum velocities are recalculated using the alternate expressions

$$\begin{aligned}\delta'_{\text{bias}}(x,z) &= v(x,z) - \frac{J_x(x,z)}{\sigma(z)F_z} - \overline{\delta'_{\text{bias}}}(x)\\ \overline{\delta'}_{\text{bias}} &= \frac{1}{H_2 - H_1}\int_{-H_1}^{-H_2}\left[v(x,z) - \frac{J_x(x,z)}{\sigma(z)F_z}\right]\mathrm{d}z\\ \delta'_{\text{std,bias}} &= \left(\frac{1}{H}\int_{-H}^{0}\delta'^2_{\text{bias}}\,\mathrm{d}z\right)^{1/2}.\end{aligned} \tag{12}$$

The integration limits used here are chosen to represent an XCP referenced with shipboard ADCP, $H_1 = -300$ m and $H_2 = -50$ m, although similar results are obtained for limits representative of other methods of referencing [*Sanford et al.*, 1985; *Szuts*, 2004].

3.2.3. Horizontal Averaging Scales

[37] Aside from its magnitude, the horizontal distance that the perturbation $\overline{\delta}$ or δ'_{std} spreads is one way to consider the shape of the perturbation. Because the perturbations are forced to follow the width scale of topographic slopes within $|x| < L_t$, passive spreading is calculated outside of this region.

[38] The half width is defined as the distance away from the origin in which the perturbation at $x = \pm L_t$ is reduced by half. This is denoted $L_{\overline{\delta}}$ and $L_{\delta'}$ for the depth-uniform and depth-varying perturbations.

4. Sloping Topography

[39] The geometry is solved with the Model for Ocean ElectroDynamics (MOED) [*Tyler et al.*, 2004]. It is a three-dimensional (3-D) model that solves Maxwell's governing electromagnetic equations in the frequency domain by finite difference for the electric and magnetic gauge potentials.

4.1. Solution Method

[40] A 2-D configuration is used by MOED to solve the geometry given. Discretizing the analytic geometry with continuously sloping boundaries to a Cartesian grid requires some care to avoid numerical difficulties.

[41] The following techniques help to minimize numerical noise: resolving the thinnest layer (the surface jet or sediment layer) by >20 grid points in the vertical, extending the jet far beyond $x = \pm L_t$ but before the end of the model domain, and vertical smoothing of the density interfaces. For the water/sediment and sediment/crust interfaces the conductivity over four grid points in the vertical is smoothed based on the exact interface depth H_i (either $-H(x)$ or $-H_s(x)$) according to

$$\begin{aligned}\sigma(z_i) = \frac{1}{2}\left[1 + \sin\left(\frac{2\pi(z_i - H_i)}{4\Delta z}\right)\right]\\ \cdot(\sigma_{\text{up}} - \sigma_{\text{lo}}) + \sigma_{\text{lo}},\end{aligned} \tag{13}$$

where z_i is within two grid points of the depth of H_i, Δz is the vertical grid spacing (Δz depends on A_t, H_{mid} and ΔH_s), and σ_{up} and σ_{lo} are the conductivities of the upper and lower layers.

[42] If the grid spacing Δx or Δz is too large, such as for very large width scales or very thin sediment layers, the perturbations from 1-D theory are dominated by grid scale noise. Practically, computational limitations on the maximum grid size prevent aspect ratios smaller than $H_{\text{mid}}/L_t = 0.03$ or sediment thinner than $\Delta H_s/H_{\text{mid}} = 0.03$. In particular, the lowest and leftmost two data points in Figures 3a and 3c require larger grid sizes (smaller grid spacing) than is solvable with the computing resources available.

[43] Validation of MOED itself is demonstrated by *Tyler et al.* [2004] for 1-D, 2-D, and 3-D cases that have analytical solutions. The particular 2-D implementation used here is cross validated with the cosine jet solution using a finite Fourier expansion [SzI, Appendix B]. The RMS difference between E_x calculated by MOED and by the Fourier expansion is 0.37% of the maximum electric field for a set of parameters that generates a strong 2-D perturbation.

4.2. Representative Example

[44] The example in Figure 2 has the parameters $L_t = 3.2$ km, $A_t = 350$ m, $H_{\text{mid}} = 1000$ m, $H' = 325$ m, $\Delta H_s = 1000$ m, and $\sigma_r = 0.1$. The sloping bottom is 10° over the central portion of the topographic relief. The bottom slope results in electric currents flowing down the slope in the water column, as seen by how J_x isolines bend from vertical to intersect $H(x)$ closer to parallel. With a shallower slope, the 1-D approximation would be more accurate along the slope and J_x would approach horizontal.

[45] The depth-averaged velocity (black line, Figure 2b) varies in tandem with $H(x)$, and $\lambda_{2\text{-D}}$ is larger on the shallower side because the sediment layer is thicker relative to water depth.

[46] Smoothing σ vertically across conductivity interfaces introduces ambiguity in the vertical limits of the integrals that define $\overline{\boldsymbol{v}}^*$ and derived quantities. The physical requirement that $\overline{\boldsymbol{v}}^*_{2\text{-D}}$ attain a constant value far from topography is met on either side of the slope. In order to not introduce errors arising from the improper representation of the geometry on the model grid, the reference quantity $\overline{\boldsymbol{v}}^*_{1\text{-D}}$ necessary for defining 2-D perturbations is defined heuristically from the model solution. The numerical $\overline{\boldsymbol{v}}^*_{1\text{-D}}$ is set to the asymptote of $\overline{\boldsymbol{v}}^*_{2\text{-D}}$ on either side, and the variation of $\overline{\boldsymbol{v}}^*_{1\text{-D}}$ across the slope is calculated from the prescribed shape of $H(x)$.

[47] The quantities $\overline{\boldsymbol{v}}^*_{2\text{-D}}$ and $\overline{\boldsymbol{v}}^*_{1\text{-D}}$ are very close, their difference as $\overline{\delta}$ (Figure 2c, solid line) is at most 0.001 m s^{-1}. $\overline{\boldsymbol{v}}^*_{2\text{-D}}$ is larger (smaller) than $\overline{\boldsymbol{v}}^*_{1\text{-D}}$ on the upper (lower) part of the slope. The depth-uniform error is 0.00068 m s^{-1}.

[48] For comparison, the transport error from a submarine cable is also shown (dash-dotted line, Figure 2c). Submarine cables integrate the electric field on the seafloor across their length. The cable error is calculated as the difference between the horizontal integrals of $E_x(1 + \lambda_{1\text{-D}})/F_z$ and the exact quantity $v(x)$, normalized by the total transport of the jet and divided by 10 for display purposes. The near-seafloor E_x is not symmetric for this geometry, such that a 1% error results for a cable that fully spans the slope.

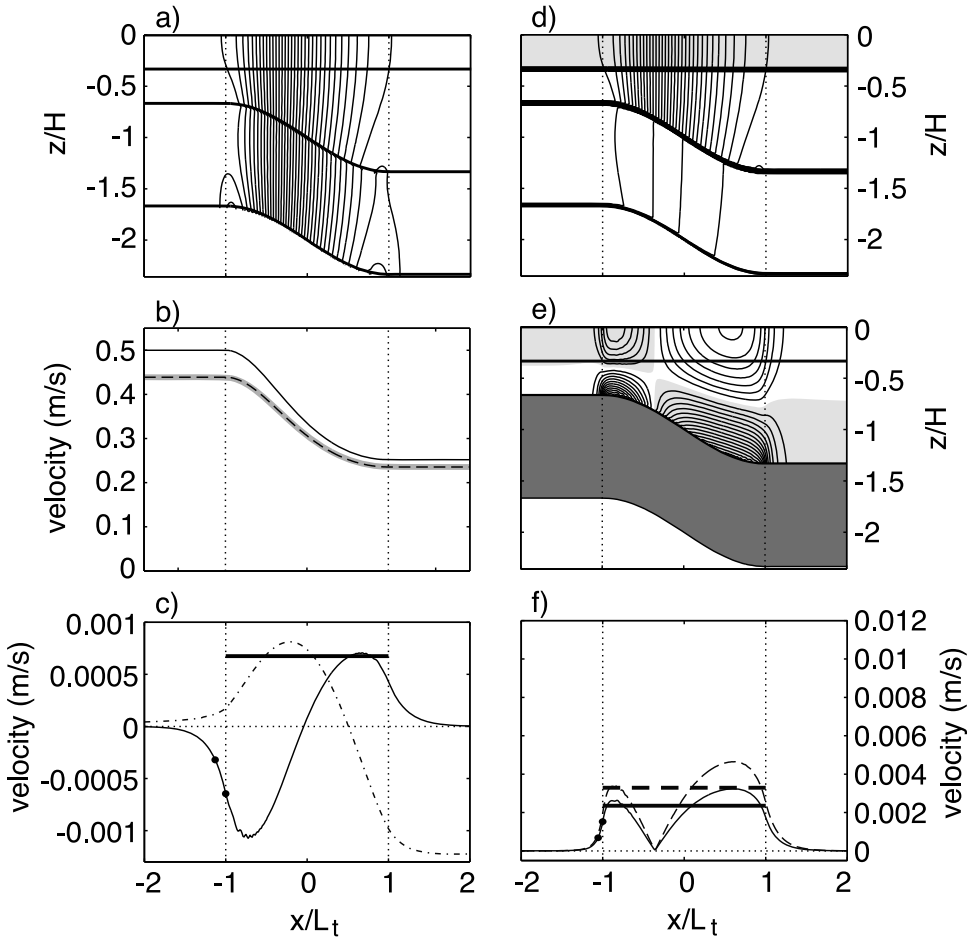

Figure 2. Solution induced by F_z for a representative case of the geometry with sloping topography with $H_{\mathrm{mid}}/L_t = 0.31$. The (left) depth-uniform and (right) depth-varying components are shown. (a) Electric field E_x, contours every 0.25 μV m^{-1}. (b) Depth-averaged velocity $\overline{\boldsymbol{v}}$ (solid black), $\overline{\boldsymbol{v}}^*_{1\text{-D}}$ (thick gray), and $\overline{\boldsymbol{v}}^*$ (dashed black). (c) Velocity perturbation $\overline{\delta}$ (thin solid) and error ϵ (thick solid), and the cable error divided by 10 (see text, dash-dotted). (d) Electric current density J_x, contours every 1 μA m^{-2}. (e) Depth-varying perturbation δ', contours every 0.0005 m s^{-1}. (f) For the depth-varying perturbations δ'_{std} (solid) and the biased perturbations (dashed), the vertical second moment $\delta'_{\mathrm{std}}(x)$ (thin) and depth-varying error ϵ' (thick). Dots in Figures 2c and 2f show the end points of the half-width decay length. The solution is for a small width slope defined by $L_t = 3.2$ km, $A_t = 350$ m, $H_{\mathrm{mid}} = 1000$ m, $H' = 325$ m, $\Delta H_s = 1000$ m, and $\sigma_r = 0.1$, which has a maximum bottom slope of 9.8°. The dashed vertical lines show the edges of the topographic slope.

[49] As with the cosine jet geometry of SzI, the depth-varying errors are intensified near the water surface and near the seafloor (Figure 2e), with a little spreading of the velocity error beyond the slope (Figure 2f). The magnitude of δ'_{std} is below 0.004 m s^{-1} (thin solid thin), and the error ϵ' is 0.0024 m s^{-1}. The biased quantities for surface-referenced profiling floats are 50% larger but remain below 0.005 m s^{-1}.

4.3. Parameter Space

[50] Because of the difficulty of visualizing a five-dimensional parameter space, three 2-D spaces are chosen with the remaining 3 scales fixed (Figures 3 and 4). The remaining nondimensional parameters are selected to be in the middle of their range (see caption). The description focuses on the realistic range of H_{mid}/L_t discussed later, or $H_{\mathrm{mid}}/L_t < 10^{-0.5}$.

[51] The depth-uniform error is most dependent on L_t, with remarkably constant dependencies on the sediment thickness ΔH_s (Figure 3a), jet depth H' (Figure 3c), and topographic relief A_t (Figure 3e) over the range of H_{mid}/L_t.

[52] The depth-uniform error increases by factors of 3–6 if $\Delta H_s/H_{\mathrm{mid}}$ increases by a factor of 10, while the error increases by less than a factor of 3 if the jet depth (H'/H_{mid}) or topographic relief (A_t/H_{mid}) increase from 0.4 to their maximum value. The dependence on σ_r (not shown) is nearly linear.

[53] The depth-uniform error can also be quantified for a cable (not shown), where the value considered is the difference between the cable error (Figure 2c) at x of L_t and $-L_t$. The dependence on $\Delta H_s/H_{\mathrm{mid}}$ is very similar to that in Figure 3b except that the cable errors are 3–10 times smaller, which implies an unexpectedly weak dependence on ΔH_s for this depth-uniform response. There is weak

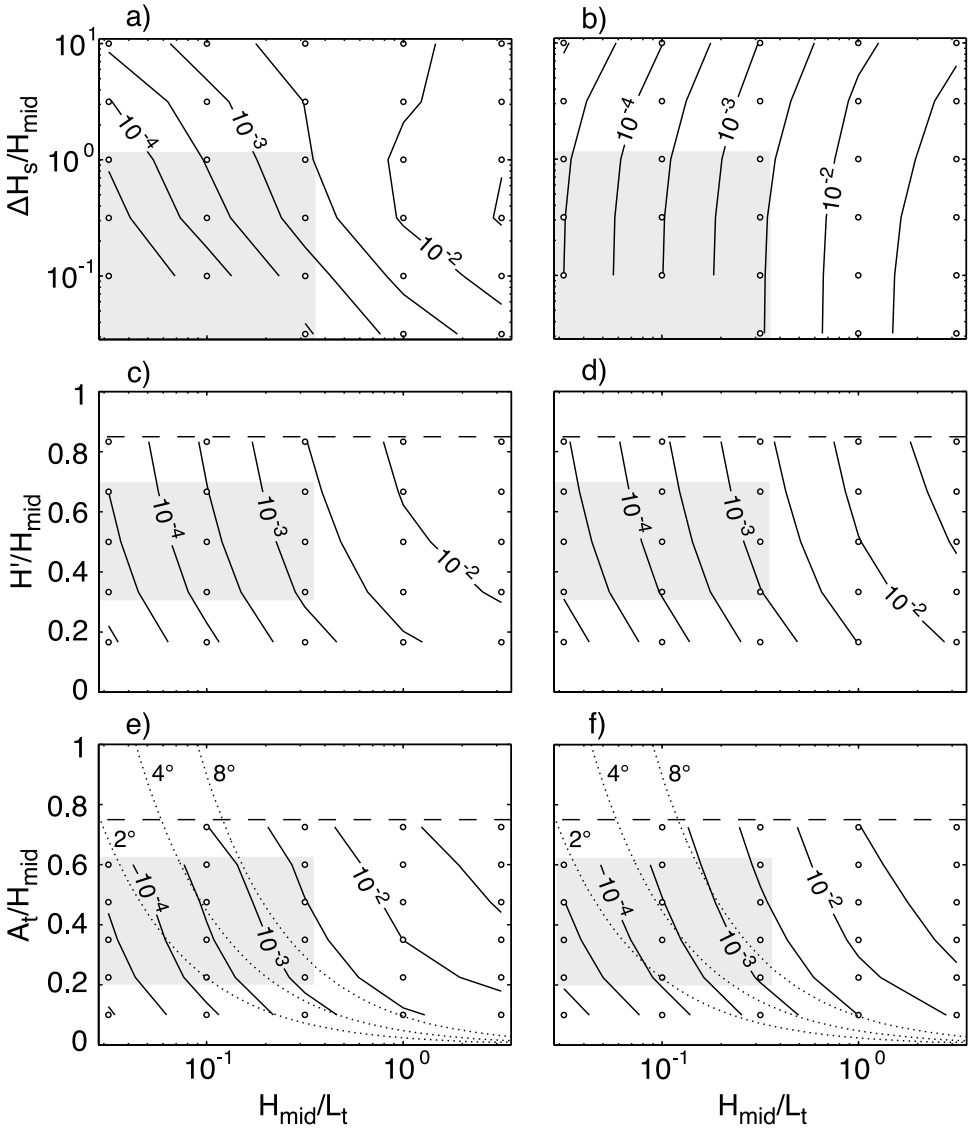

Figure 3. Parameter space representation of velocity errors induced by F_z from the geometry with sloping topography. The (left) depth-uniform error and (right) depth-varying error plotted against H_{mid}/L_t for (top) $\Delta H_s/H_{mid}$ (with H'/H_{mid} = 1/3, A_t/H_{mid} = 1/3, σ_r = 0.1), (middle) for H'/H_{mid} (with $\Delta H_s/H_{mid}$ = 1, A_t/H_{mid} = 0.15, σ_r = 0.1), and (bottom) for A_t/H_{mid} (with $\Delta H_s/H_{mid}$ = 1, H'/H_{mid} = 0.25, σ_r = 0.1). In Figure 3 (middle) and Figure 3 (bottom), the upper limit of H'/H_{mid} and A_t/H_{mid} is shown by the long dashed line, as constrained by A_t/H_{mid} = 0.15 or H'/H_{mid} = 0.25. Figure 3 (bottom) also include the maximum slope angle in degrees (dotted). Data points not shown are biased by numerical noise. Shading indicates the region over which the error is fit (see Table 1).

dependence on H', and the cable error is roughly 3 times larger than shown in Figure 3c. The largest dependence of the cable error is to A_t/H_{mid}; the errors are similar to those in Figure 3e except roughly 10 times larger.

[54] The depth-varying velocity error ϵ' (Figures 3b, 3d, and 3f) is only weakly influenced by ΔH_s, except for very large thickness ($\Delta H_s/H_{mid} \geq 30$). Jet depth H' and topographic relief A_t change ϵ' by less than a factor of 3 when they occupy more than 40% of H_{mid}. For any resolved value of H'/H_{mid}, errors vary by at most a factor of 3, while for any resolved value of A_t/H_{mid} the errors vary by less than a factor of 10.

[55] Over the resolved parameter space, both depth-uniform and depth-varying errors are $\leq$0.001 m s^{-1} solely if $H_{mid}/L_t \leq 0.1$.

[56] The errors ϵ and ϵ' for sloping topography are fit to functions of the form

$$\left(\frac{H_{mid}}{L_t}\right)^a \left(\frac{Y}{H_{mid}}\right)^b c \tag{14}$$

over the region of the parameter space shown by gray shading in Figure 3, where Y is one of ΔH_s, H', or A_t (Table 1). Generally, all errors depend on H_{mid}/L_t to the power of 1.9. The sediment thickness has less of an effect

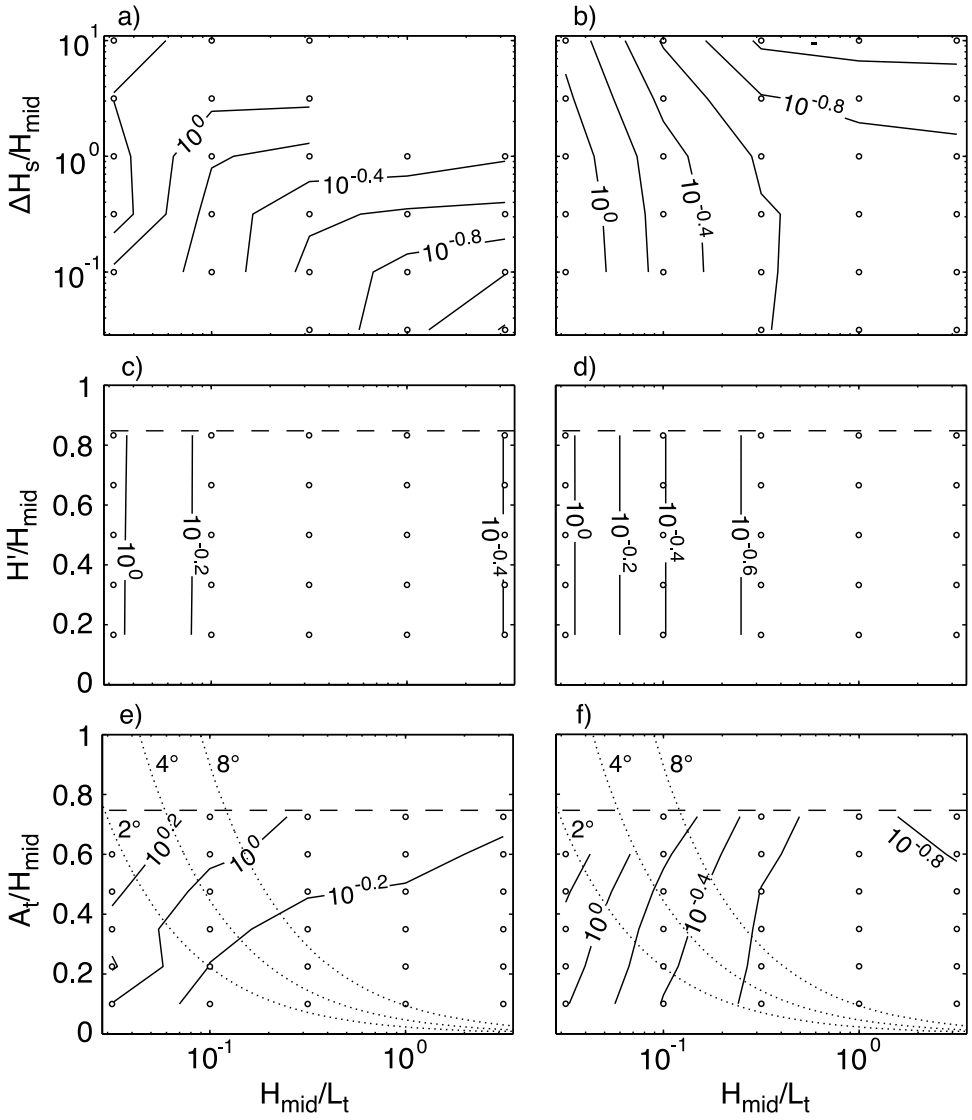

Figure 4. Half-widths (left) $L_{\bar{\delta}}$ and (right) $L_{\delta'}$ normalized by the $D_{1\text{-D}}$ that is calculated on the shallower side of the slope. Other aspects are the same as in Figure 3.

($b < 1$) on the depth-uniform error, but has almost no effect on the depth-uniform error. For H' and A_t the dependence is roughly linear (a power of 1).

[57] The half width of depth-uniform perturbations $L_{\bar{\delta}}$ (Figure 4) depends on the aspect ratio, the sediment thickness, and the topographic amplitude in order of importance. Like for the cosine jet [SzI], for thin (thick) sediment $L_{\bar{\delta}}$ varies most with H_{mid}/L_t ($\Delta H_s/H_{mid}$), except that the demarcation line is where they are inversely related (power of −1). There is no dependence on H', and $L_{\bar{\delta}}$ varies by only 2–3 over the full range of A_t. For narrow slopes the values are tenths of $D_{1\text{-D}}$, whereas for wider slopes the widths are 1–2 $D_{1\text{-D}}$.

[58] The half width of depth-varying perturbations $L_{\delta'}$ is very similar to the cosine jet case [SzI, Figure 6b], except that slightly larger values (1 $D_{1\text{-D}}$) are reached at $H_{mid}/L_t = 10^{-1.5}$. There is still no dependence on H', and that of A_t remains a factor of 2–3 over the full range of A_t. As with $L_{\bar{\delta}}$, $L_{\delta'}$ only obtains a maximum of 1–2 $D_{1\text{-D}}$ at the smallest resolved aspect ratios and doesn't appear to approach an asymptote.

5. Discussion

[59] Overall, this study aims to address the relative importance of 2-D perturbations in motionally induced signals that arise in the presence of sloping topography. Our approach isolates the 2-D errors in calculating velocity from $\boldsymbol{E}$ and $\boldsymbol{J}$ on the basis of nondimensional scales. Additional context is necessary for understanding the physical implications of these results and their extension to different situations. Before the results are generalized, the nondimensional parameters must be constrained to realistic ranges and salient features of the geometry are discussed as a guide for extrapolating our results to different geometries.

[60] The discussion seeks the general nature of the results and their implications for observations. This is done by discussing: the physical explanation, the sensitivity, and the

Table 1. Fits of the Velocity Errors ϵ or ϵ' to (14) Over the Regions in Figure 3 Indicated by Gray Shading[a]

Error	Y	a	b	c	Relative RMS Error
ϵ	ΔH_s	1.87	0.68	0.026	0.15
ϵ	H'	1.89	0.99	0.033	0.04
ϵ	A_t	1.92	1.14	0.069	0.08
ϵ'	ΔH_s	1.95	−0.08	0.023	0.03
ϵ'	H'	1.94	0.99	0.028	0.02
ϵ'	A_t	1.95	1.23	0.066	0.02

[a] Y stands for the nondimensional parameter listed. The relative RMS error of the fit is calculated as RMS $(\epsilon/\epsilon_{\text{fit}} - 1)$. The coefficients are accurate to a few percent or less, a and b are dimensionless, c has the dimensions of velocity, and all fits have $R^2 \geq 0.994$.

magnitude of 2-D perturbations; how to apply the errors defined here for different observational techniques; and lastly how velocity gradients [SzI] and topographic slopes interact in the generation of 2-D perturbations by application of our results to specific observations.

5.1. Constraints on Aspect Ratios and Other Parameters

[61] The schematic geometries were chosen to facilitate a parameter-space analysis and were not constrained to be realistic a priori. Limitations from geological observations are discussed next to define the realistic region of the parameter space.

[62] Geophysically stable slopes can be constrained by observations, or perhaps by stability arguments. Most instabilities that limit the slope are hard to generalize due to their infrequent occurrence and spatial heterogeneity, however, e.g., elevated pore pressure, turbidity currents, earthquakes, or internal wave critical reflection [see *Cacchione et al.*, 2002; *Lee et al.*, 2007], so it is easier to consider slopes that occur in nature. Because the slope has to have a significant vertical extent compared to the water depth to appreciably change the EM response, only topographic features that are a significant fraction of the water depth are considered. The geologic literature discusses slope angle $\theta = \tan^{-1}(\Delta z/\Delta x)$ instead of $\Delta z/\Delta x$ or A_t/L_t. For reference, contours of the angle at $x = 0$, or $\tan^{-1}(\pi A_t/2L_t)$, are shown in Figures 3e and 3f (dotted line).

[63] Sedimented continental slopes typically have slopes from 5° for unstable margins (tectonically active or salt tectonized) to 8° for passive margins [*Pratson and Haxby*, 1996]. For volcanic topographic features, median slopes of 4–5° are found around the Hawaii Ridge, with maxima of 8–12°, while the Mendocino Escarpment transform fault has a mean and maximum slope of 11° and 15° (from bathymetry with 3 km resolution) [*Smith and Sandwell*, 1997].

[64] There are two other geologic parameters, sediment thickness and sediment electrical conductivity, for which observed values are briefly presented. Total sediment depths from a global composite [*Laske and Masters*, 1997] range from 0 over newly formed oceanic crust to up to 10 km deep in old sedimentary basins. Passive sedimented margins typically have sediment thicknesses of 4–8 km within 100 km of the continental slope, while subducting margins have thicknesses of 1–4 km.

[65] Sediment conductivity is largely determined by porosity, because saltwater is the most common pore fluid (for more detailed treatment see *Simpson and Bahr* [2005] and *Szuts* [2008]). Conductivities of specific sediment types and layers can vary from $\sigma_r \sim 0.025$ ($\sigma_s = 0.1$ S m^{-1}) for low-porosity consolidated silt to $\sigma_r \sim 0.5$ ($\sigma_s = 1.5$ S m^{-1}) for sandy unconsolidated deposits. In general, conductivity decreases exponentially with depth in the sediment via Archie's Law [*Flosadóttir et al.*, 1997]. Thus, the influence of the sediment layer on the electric field through $\lambda_{1\text{-D}}$ is through an apparent conductivity that is a vertical weighting of the depth-varying conductivity. In the presence of 2-D perturbations, conductive surficial sediment layers will act to increase the sediment shorting more than homogeneous sediment.

5.2. Limitations of Resolved Geometries

[66] Although the geometry was chosen to be broadly applicable, there are a four limitations to note for applying our results to other situations and geometries.

[67] 1. A surface layer in slab motion is unrealistic. This choice was made to allow a parameter space analysis, but in reality the interaction of topography and velocity is much more complex (see section 5.5).

[68] 2. The two layer ocean flow describes a vertical step change in velocity. This sharp boundary maximizes the vertical second moment of velocity error. Smoother vertical structure will generate smaller depth-varying errors.

[69] 3. The choice of uniform conductivity in the ocean layers ignores salinity stratification. The small range of conductivity in the open ocean leads to a small distortion that is corrected with the factor γ (<10% for open ocean modes [*Chave and Luther*, 1990]).

[70] 4. The geometry chosen has a nonzero depth-averaged velocity, so care needs to be taken when extending these results to the predominantly depth-varying (or baroclinic) flow often measured with profiling floats. In particular, this analysis can't distinguish the relative contributions of the depth-averaged and depth-varying velocity forcing to the depth-varying response J_x. It is difficult to generalize baroclinic flows because internal modes or waves have small vertical structure, propagate at an angle in the vertical, and have a wide range of horizontal coherence (whether a mode or beam), implying that length scales in both horizontal directions must be considered.

5.3. Physical Meaning, Sensitivity, and Magnitude of 2-D Perturbations

[71] The example shown in Figure 2 uses an aspect ratio representative of continental shelves. To illustrate the 2-D perturbations in general, however, unrealistically narrow width scales are necessary to accentuate the changes. The perturbations induced by F_z are illustrated in Figure 5 with an electric current stream function ψ (Figure 5, top, defined as $\nabla \times \hat{\boldsymbol{j}}\psi = \boldsymbol{J}$) and by the electric potential ϕ (Figure 5, bottom). The stream function is calculated numerically in Matlab.

[72] When the sea floor is not horizontal but the topographic aspect ratio is small (nearly 1-D case), the electric currents follow the slope (Figure 5a). Streamlines enter the sediment smoothly via the 1-D approximation in close relation to how $\bar{\boldsymbol{v}}$ increases as the bottom shoals. Vertical isopotentials demonstrate that electric currents are almost entirely horizontal (Figure 5c). In the presence of a steep

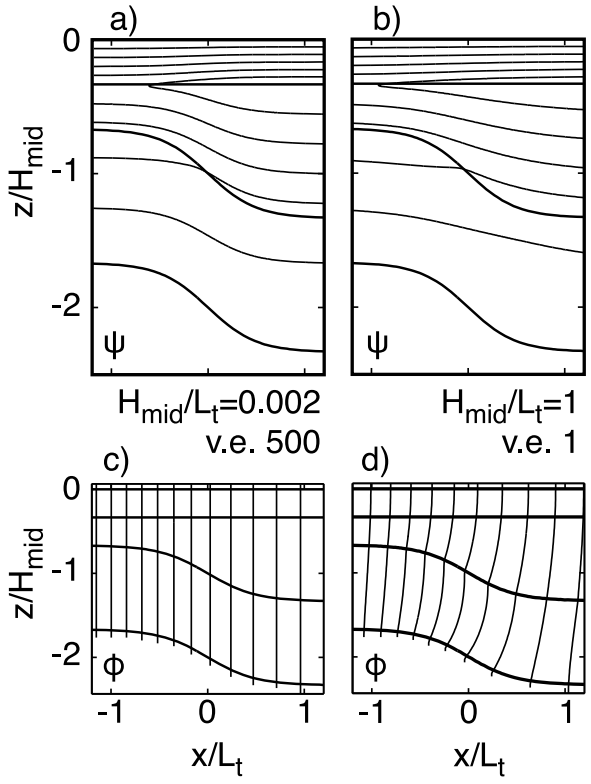

Figure 5. The 2-D perturbations in (top) the electric current stream function ψ and (bottom) the electric potential ϕ induced by F_z for small and large topographic aspect ratios. (left) A nearly 1-D response ($H_{mid}/L_t = 0.002$, vertical exaggeration of 500) contrasts with (right) a strongly 2-D response ($H_{mid}/L_t = 1$, no vertical exaggeration). (a and b) The quantity ψ is calculated numerically in Matlab and is not exactly evenly spaced, while (c and d) ϕ calculated with MOED has contour spacings of 0.2 V (Figure 5c) and 0.0025 V (Figure 5d). Unspecified nondimensional parameters are the same as in Figure 7 from SzI, which describes 2-D perturbations caused by horizontal velocity gradients.

slope, electric currents refract when they enter the sediment and don't uniformly fill the water or sediment layers near $x/L_t = \pm 0.5$ according to the 1-D approximation (Figure 5b). This effect can be seen more clearly in Figure 2, where negative (positive) velocity perturbations δ' at the seafloor correspond to positive (negative) depth-uniform error $\overline{\delta}$. In the bottom of the water column isopotentials are tilted to intersect the seafloor closer to perpendicular (Figure 5d), resulting in a weakening of E_x close to the sediment. Extrema in the depth-uniform and depth-varying errors occur at the upper and lower parts of the slope.

[73] The parameter space analyses show that there is a transition point in the velocity errors below H_{mid}/L_t of 0.5–1, which is also a transition point for velocity aspect ratios [SzI]. That the realistic range of topographic slopes occurs for $H_{mid}/L_t \leq 1$ allows the errors to be described as powers of the nondimensional parameters.

[74] All errors depend on H_{mid}/L_t to the power of 1.9. As a point of comparison, the dependence suggested by *Sanford* [1971] for topographic aspect ratios is less specific as it is a mix of topographic and velocity scales. His perturbation analysis assumed that perturbations scale as A_t/L in our notation (L being the oceanic or velocity width scale) and then found that terms involving ∇H scale as the oceanic aspect ratio H/L. Depth-uniform errors depend on the sediment conductivity to the power of one and on sediment thickness to the power of 0.7. The dependence is thus proportional to $\lambda_{1\text{-D}}$ to a power slightly less than one, in contrast to the near-linear proportionality on $\lambda_{1\text{-D}}$ for perturbations generated by velocity gradients [SzI]. On the other hand, depth-varying errors are nearly independent of sediment thickness and conductivity. Lastly, the depth of the jet and the topographic amplitude both lead to a power one proportionality for both depth-uniform and depth-varying errors.

[75] For the same aspect ratio ($H/L = 0.1$ or $H_{mid}/L_t = 0.1$), depth-varying errors generated by topography (0.00015 m s^{-1}) are an order of magnitude smaller than those generated by velocity gradients (0.003–0.015 m s^{-1}). For steeper continental slopes ($H_{mid}/L_t = 0.3$ and $A_t = 1/3$, or 8°) the errors are less than 0.01 m s^{-1}.

[76] The effective horizontal averaging distance is 0.2–1.2 $D_{1\text{-D}}$ for all parameter spaces considered. Consistent with the findings of SzI, the half widths do not approach an upper asymptote at the lowest resolved values H_{mid}/L_t. This reflects the dominance of the forcing width scale at small aspect ratio, is consistent with *Chave and Luther* [1990], and suggests that $D_{1\text{-D}}$ is the scale over which motionally induced signals are horizontally averaged in the ocean.

5.4. Application to In Situ Observations

[77] The definition of the velocity errors as either depth-uniform $\overline{\epsilon}$ or depth-varying $\overline{\epsilon'}$ decouples these two modes from each other for the analyses performed here and in the work of SzI. Full water column averaging was used to calculate $\overline{\boldsymbol{v}}^*$ and $\overline{\epsilon'}$ from the 2-D solutions, but full water column averages are not typically used for measurements. Stationary electrodes measure E_x at one point in the vertical, or vertical profiling floats are referenced to absolute velocity over some fraction of the water column. In general, the perturbation at the depth of the sensor is $E_x(z)/F_z - \overline{\boldsymbol{v}}^*_{1\text{-D}}$, which is equivalent to $\overline{\delta} + \delta'(z)$. In the center of the water column the in situ observations are in error by ϵ, whereas close to the sea surface or the seafloor there is an additional contribution from the depth-varying perturbation. Referencing vertical profilers over a fraction of the water column increases the velocity errors by 25–60%. Biased errors caused by midlevel or near-bottom referencing have similar dependencies.

[78] Further difficulties arise in practice due to a lack of sediment knowledge. The perturbations calculated here presuppose complete knowledge of $\lambda_{1\text{-D}}$, which is generally poorly known. Although velocity errors are very small if λ is calculated heuristically with $\overline{\delta}_{emp}$, the smooth geometries and noise-free analysis is not appropriate for quantifying such errors. Sz10 investigates the issue of unknown sediment electrical properties at a complex location.

5.5. Combined Effect of Velocity and Topographic Gradients

[79] Between this article and SzI the independent roles of velocity gradients and sloping topography on generating 2-D EM perturbations are analyzed, but this separation is

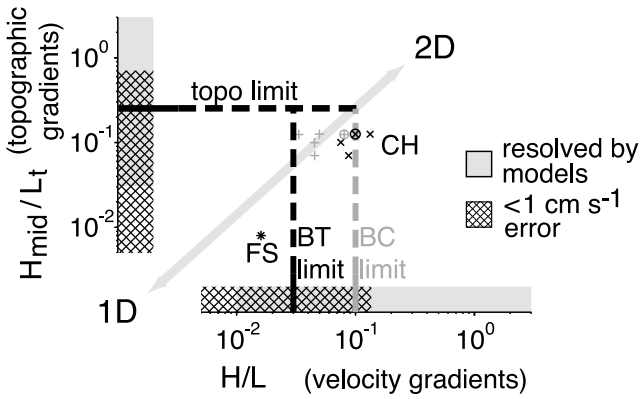

Figure 6. Schematic representation of the parameter space. The abscissa summarizes the geometry with velocity gradients [SzI], while the ordinate summarizes the geometry with topography (section 4). In each, aspect ratios yielding errors smaller than 1 cm s^{-1} are shown with crosshatching for $(H_s - H)/H \leq 1$, $\Delta H_s/H < 1$, and $\sigma_r = 0.1$. The nominal limits for aspect ratios are shown with thick lines labeled BT (depth-averaged velocity), BC (depth-varying velocity) or topo (topographic). For reference, the parameter space location of the Florida Straits cable (denoted FS) and of 5 stations in the Gulf Stream at Cape Hatteras (denoted CH) are also plotted. The Cape Hatteras stations differentiate between the baroclinic component (gray pluses) and the barotropic component (black crosses, two points are identical) at which 2-D electric fields are investigated by Sz10. Values for the station at 500 m are circled.

often not possible in the real ocean. Represented graphically (Figure 6), our results only apply along each axis separately. The regions where depth-uniform and depth-varying velocity errors are less than 0.01 m s^{-1} are shaded, assuming typical values of $(H_s - H)/H \leq 1$, $\sigma_r = 0.1$, $H'/H = 0.5$, and $A_t/H_{mid} = 0.5$. Thick lines show the expected upper limits from the discussions, where dashed lines indicate the qualitative nature of the discussion when both steep topography and sharp velocity features are present. For small gradients, the combined velocity errors in the presence of both gradients may be described by linear addition, but in general topographic and velocity gradients will interact nonlinearly both in setting the flow field and in the magnetostatic response. Not only does topography impose strong constraints on geostrophic flow, but it also separates regions of different dynamics (e.g., shelf circulation and ocean-basin boundary currents).

[80] The extrapolation of our generalized results to situations with both topography and velocity gradients, that is, the real ocean, is not straightforward. Two separate examples serve as a guideline to do so: the Florida Straits, a location of long-standing cable measurements [*Larsen and Sanford*, 1985]; and the Cape Hatteras region studied by Sz10.

[81] In the Florida Straits, the voltage across a seafloor cable provides a highly accurate proxy for transport [*Larsen and Sanford*, 1985; *Shoosmith et al.*, 2005]. Because the local sediment properties, the removal of geomagnetic and tidal signals, and the implications of how the cable integrates horizontally along its length have been well treated by previous work [*Spain and Sanford*, 1987; *Larsen*, 1992], here we simply add the implications of our result for interpretation of the cable voltage in terms of the time-averaged velocity structure of the Florida Current. Meanders of the current axis, eddies close to the Florida coastline, or other fine scale and quickly evolving variability fall outside of our treatment.

[82] Two-dimensional perturbations should be largest along the sloping west side of the channel, which is approximately linear over 50 km to the maximum depth of 750 m (a slope of 0.8°). The thick sediment results in a factor 2 reduction of $\overline{\boldsymbol{v}}^*$ compared to $\overline{\boldsymbol{v}}$, also implying that the vertical governing scale $D_{1\text{-}D}$ is roughly twice the (local) water depth, or always ≤1.5 km. The topographic aspect ratio of the strait is 750 m/90 km = 0.008, while the velocity aspect ratio is roughly twice this value (0.015) because the main transport occurs in the central part of the strait.

[83] For the depth-uniform signal that the cable responds to, the local 2-D perturbation is expected thus to be very small due to either topography (≤10^{-5} relative error) or due to velocity gradients (≤10^{-4} relative error). Since the cable integrates perturbations along its length and extends entirely across the strait, 2-D errors due to velocity gradients are expected to largely cancel. Cable errors due to the sloping topography, though nonzero when integrated across one slope, are also expected to cancel given that the channel can be considered as two slopes of opposite relief.

[84] The observations at Cape Hatteras analyzed by Sz10 were collected to test the 1-D approximation of motional induction [*Sanford et al.*, 1996]. This data was collected across the Gulf Stream at Cape Hatteras, where velocity is strong and subject to sharp fronts, the continental slope is unusually steep, and sediments are thick and heterogeneous.

[85] First, the nondimensional parameters at the 500 m station are needed: local approximations are made to the parameters defined for the schematic geometries. The width scale is the width of the velocity maximum on the upper continental shelf (L = 5 km), the effective sediment conductivity comes from the best-fit forward electric field numerical calculation (σ_s = 0.58 S m^{-1}), and the other scales are evident from transect geometry, velocity, and CTD data: H = 500 m, depth of Gulf Stream H' = 400 m, center of continental slope H_{mid} = 1250 m, width of slope L_t = 10 km, sediment thickness ΔH_s = 5 km, half the topographic relief A_t = 1200, and average water conductivity $\overline{\sigma}$ = 4.2 S m^{-1}. The nondimensional scales are thus $H/L = 0.1$, $H'/H = 0.8$, $H_{mid}/L_t = 0.125$, $(H_s - H)/H = 10$, $\sigma_r = 0.14$, and $A_t/H_{mid} = 0.96$.

[86] With these parameters, it is seen that the 500 m station is indeed in an extreme corner of the parameter space (circled points in Figure 6). By a similar analysis, the remaining 4 stations (labeled CH) are also in the extreme 2-D part of the parameter space. The barotropic aspect ratios at Cape Hatteras are larger than expected from the discussion of velocity aspect ratios in the work of SzI, which is attributed to the incongruence between the definition of nondimensional parameters from the schematic geometries, the actual geometry at Cape Hatteras, and the simplified discussion of geophysical dynamic constraints.

[87] As the sediment thickness is outside the range fit with powers of the nondimensional parameters (Table 1 and Table 1 of SzI), the errors graphed need to be corrected

Table 2. Expected Velocity Errors at the 500 m Station in a Transect SE of Cape Hatteras[a]

	Depth Uniform (m s^{-1})	Depth Varying (m s^{-1})
Velocity gradient, F_z	0.17	0.0089
Velocity gradient, F_x	0.018	0.038
Topographic gradient, F_z	0.013	0.0012
Cape Hatteras, 500 m isobath	0.20	0.03
Cape Hatteras, other isobaths	0.01–0.05	0.01–0.02

[a]See text. The Cape Hatteras values (Sz10) are not RMS errors as are the velocity and topographic gradients, instead they are the single-value (maximum) errors for the depth-uniform (depth-varying) signals.

using the fit sensitivities. Note that the errors shown for the 500 m station are not equivalent to the spatial RMS errors discussed here, instead they are single values (maximum values) of the depth-uniform (depth-varying) errors.

[88] The expected error generated by velocity gradients is read off of Figure 5 of SzI for $H/L = 0.1$ and $(H_s - H)/H = 10$, which is 0.10 m s^{-1}. This value then needs to be corrected for the different values of H' and σ_r, yielding (0.10 m s^{-1}) $(0.8/0.5)^{0.44}$ $(0.14/0.1)^{1.02}$ = 0.17 m s^{-1}.

[89] The expected error from sloping topography are calculated in a similar fashion. The same σ_r dependence is used as found for the velocity gradients. The topographic relief of 0.96 is well outside of the resolved range, for which it is clear that the power dependence on A_t/H_{mid} increases beyond the value of 1.2 found for $0.23 \leq A_t/H_{\mathrm{mid}} \leq 0.6$. Because the actual geometry of the Gulf Stream is too complex to be compared directly to the slab motion in the topographic schematic geometry, a value of 2 is used for application to the 500 m station at Cape Hatters.

[90] The same procedure is used to calculate the expected depth-varying errors. A further correction necessary is that the profiling instrument used in Sz10 is only referenced within 200 m of the bottom, not over the full water column. Biased depth-varying errors are 20–50% larger, so the depth-varying errors enumerated above are further increased by a factor of 1.35.

[91] The largest anticipated errors from the schematic geometries (Table 2) are within 30% of the 2-D errors calculated from high resolution numerical modeling of the region assuming a time-averaged velocity structure. These results are surprisingly consistent given that the simplified geometries are far from analogous to the range of nondimensional scales present at the 500 m station.

[92] It is unclear how to combine the 3 anticipated errors further: although there is a clear relationship between the sign of the errors in the simple geometries, it is not apparent how to estimate whether the errors are in phase or not at the 500 m station. In the absence of a way to estimate the joint 2-D error generated by velocity gradients and sloping topography, these results suggest that F_z-induced perturbations from velocity gradients are mostly responsible for the depth-uniform error from Sz10, whereas F_h-induced perturbations from velocity gradients are mostly responsible for the depth-varying error. Although the 500 m isobath station occupies the most extreme set of parameters and has the largest modeled 2-D errors, at other stations the errors are a few cm s^{-1}.

[93] There are two other ways in which the 1-D approximation can be perturbed that are beyond the scope of the the 2-D parameter space investigated here: depth-uniform nonlocal currents generated by 3-D geometries, and large-scale tidal velocities. The former require high resolution numerical models to resolve the steep topography and fast mesoscale activity that will generate the largest nonlocal currents. Lower limits are suggested by 1° resolution numerical models with monthly averaged velocities [*Tyler et al.*, 2004; *Vivier et al.*, 2004; R. H. Tyler et al., personal communication, 2007]. Given the similar dependence of non-1-D perturbations on velocity and topographic aspect ratios, nonlocal currents are expected to have a similar dependence when the length scales are small in both horizontal directions. The periodic forcing of tidal velocities is measurable on a large scale by satellite magnetometers [*Tyler et al.*, 2003] and is treated generally by *Chave and Luther* [1990]. Both processes, however, have not yet been investigated with in situ observations.

6. Conclusion

[94] In regions with steep topography there can be 2-D perturbations on top of the dominant 1-D motionally induced signals. This article addresses the extent to which these perturbations depend on the surrounding geometrical and electrical nondimensional parameters. More specifically, we characterize the magnitude and sensitivity of 2-D perturbations generated by sloping topography. The parameter with the greatest influence on 2-D perturbations is the topographic aspect ratio, the mean water depth across the slope divided by the width of the slope, but there are additional contributions from the remaining parameters of sediment thickness, sediment conductivity, and the thickness of the oceanic flow.

[95] For typical values of the nondimensional parameters, the maximum errors introduced by a 1-D interpretation of the 2-D solution are less than a few percent. Over the realistic range of the parameter space (topographic slopes less than 10°, topographic relief a significant fraction of the water depth, topographic aspect ratios less than 0.3, sediments thinner than 10 times the water depth, and sediments on average 10 times less conductive than seawater) the simple shape of the 2-D velocity errors enables their sensitivity to the nondimensional parameters to be readily calculated.

[96] Both depth-uniform and depth-varying velocity errors depend on aspect ratio to the power of 1.9, depth jet to the power of 1, and topographic relief to the power of 1.2. Depth-uniform errors depend on the sediment thickness to the power of 0.7 and linearly on the sediment conductivity, which together are roughly proportional to $\lambda_{1\text{-D}}$, while depth-varying errors are nearly independent of sediment thickness. The 2-D perturbations decay away from the topography over a half width of 0.2–1 $D_{1\text{-D}}$, suggesting that this scale is a good approximation of the horizontal averaging distance for the motionally induced signal.

[97] The role of velocity gradients and topographic slope are considered separately, but if both gradients are present the resulting errors may combine nonlinearly in a manner best considered case by case. Estimates of the expected error at a field site are in good agreement with those estimated

from a detailed analysis of the site. Depth-uniform errors come predominantly from perturbations generated by velocity gradients and induced by the vertical component of the Earth's magnetic field; while depth-varying errors come predominantly from perturbations generated by velocity gradients and induced by the horizontal component of the Earth's magnetic field. Despite the steep continental slope, perturbations generated by topography are estimated to be an order of magnitude smaller.

[98] The application of these results to observations depends on the platform used to collect measurements. Stationary sensors will be subject to a depth-uniform error plus the depth-varying error at that depth, while horizontally drifting instruments such as vertical profilers will be subject to a depth-varying error whose magnitude depends on the method used for absolute referencing. The estimated errors for any particular study site can be estimated with these results prior to sampling. The order of magnitude (less than a few 0.01 m s^{-1}) of perturbations at typical locations, however, are equivalent to the accuracies of most instruments that measure velocity, whether they do so directly or using EM fields. Direct observations of 2-D perturbations are necessary to confirm the practical implications of this study.

[99] This analysis of 2-D perturbations extends existing theories from the small aspect ratio limits of both oceanic flow or topographic slope to the maximum values expected in reality. Except for sites that occupy an extreme part of the parameter space, the 1-D approximation is found to be adequate within a few percent for interpreting observations.

[100] **Acknowledgments.** This work benefitted greatly from the guidance of Tom Sanford at all stages of the project, and discussions with him, Eric D'Asaro, and James Girton brought much clarity to the final results. Rob Tyler is graciously acknowledged for the free use of his model MOED. This work was supported by NSF grant OCE 0552139.

References

Cacchione, D. A., L. F. Pratson, and A. S. Ogston (2002), The shaping of continental slopes by internal tides, *Science*, *296*(5568), 724–727.

Chave, A. D., and D. S. Luther (1990), Low-frequency, motionally induced electromagnetic fields in the ocean: 1. Theory, *J. Geophys. Res.*, *95*(C5), 7185–7200.

Chave, A. D., D. S. Luther, and J. H. Filloux (1992), The Barotropic Electromagnetic and Pressure Experiment: 1. barotropic current response to atmospheric forcing, *J. Geophys. Res.*, *97*(C6), 9565–9593.

Cunningham, S. A., et al. (2007), Temporal variability of the Atlantic meridional overturning circulation at 26.5°N, *Science*, *317*(5840), 935–938, doi:10.1126/science.1141304.

Flosadóttir, Á. H., J. C. Larsen, and J. T. Smith (1997), Motional induction in North Atlantic circulation models, *J. Geophys. Res.*, *102*(C5), 10,353–10,372.

Larsen, J. C. (1968), Electric and magnetic fields induced by deep sea tides, *Geophys. J. Int.*, *16*, 40–70.

Larsen, J. C. (1971), The electromagnetic field of long and intermediate water waves, *J. Mar. Res.*, *29*(1), 28–45.

Larsen, J. C. (1992), Transport and heat flux of the Florida Current at 27°N derived from cross-stream voltages and profiling data: Theory and observations, *Philos. Trans. R. Soc. London Ser. A*, *338*, 169–236.

Larsen, J. C., and T. B. Sanford (1985), Florida Current volume transport from voltage measurements, *Science*, *227*(4684), 302–304.

Laske, G., and G. Masters (1997), A global digital map of sediment thickness, *Eos Trans. AGU*, *78*, F483.

Lee, H. A., et al. (2007), Submarine mass movements on continental margins, in *Continental Margin Sedimentation: From Sediment Transport to Sequence Stratigraphy*, *Int. Assoc. Sedimentol. Spec. Publ. Ser.*, vol. 37, edited by C. A. Nittrouer et al., chap. 5, pp. 213–274, Blackwell, Malden, Mass.

Luther, D. S., and A. D. Chave (1993), Observing integrating variables in the ocean, in *Proceedings of the 7th Annual 'Aha Huliko'a Hawai'ian Winter Workshop on Statistical Methods in Physical Oceanography*, edited by P. Müller and D. Henderson, pp. 103–129, Univ. of Hawaii at Mānoa, Honolulu.

Pratson, L. F., and W. F. Haxby (1996), What is the slope of the U.S. continental slope?, *Geology*, *24*(1), 3–6.

Sanford, T. B. (1971), Motionally induced electric and magnetic fields in the sea, *J. Geophys. Res.*, *76*(15), 3476–3492.

Sanford, T. B., R. G. Drever, and J. H. Dunlap (1985), An acoustic doppler and electromagnetic velocity profiler, *J. Atmos. Oceanic Technol.*, *2*(2), 110–124.

Sanford, T. B., M. D. Allison, J. H. Dunlap, F. R. Stahr, and J. A. Verrall (1996), R/V Endeavor 239: Cruise report and preliminary results, *Tech. Rep. 9603*, Appl. Phys. Lab., Univ. of Wash., Seattle, Wash.

Shoosmith, D. R., M. O. Baringer, and W. E. Johns (2005), A continuous record of Florida Current temperature transport at 27°N, *Geophys. Res. Lett.*, *32*, L23603, doi:10.1029/2005GL024075.

Simpson, F., and K. Bahr (2005), *Practical Magnetotellurics*, 251 pp., Cambridge Univ. Press, Cambridge, U. K.

Smith, W. H. F., and D. T. Sandwell (1997), Global seafloor topography from satellite altimetry and ship depth soundings, *Science*, *277*(5334), 1957–1962.

Spain, P., and T. B. Sanford (1987), Accurately monitoring the Florida Current with motionally induced voltages, *J. Mar. Res.*, *15*(4), 599–608.

Szuts, Z. B. (2004), Electric field floats in the North Atlantic Current: Validation and observations, M.Sc. thesis, Sch. of Oceanogr., Univ. of Wash., Seattle, Wash.

Szuts, Z. B. (2008), The interpretation of motionally induced electric fields in oceans of complex geometry, Ph.D. thesis, Sch. of Oceanogr., Univ. of Wash., Seattle, Wash.

Szuts, Z. B. (2010), Relationship between ocean velocity and motionally-induced electrical signals: 1. In the presence of horizontal velocity gradients, *J. Geophys. Res.*, *115*, C06003, doi:10.1029/2009JC006053.

Tyler, R. H. (2005), A simple formula for estimating the magnetic fields generated by tsunami flow, *Geophys. Res. Lett.*, *32*, L09608, doi:10.1029/2005GL022429.

Tyler, R. H., and L. A. Mysak (1995a), Motionally-induced electromagnetic fields generated by idealized ocean currents, *Geophys. Astronphys. Fluid Dyn.*, *80*, 167–204.

Tyler, R. H., and L. A. Mysak (1995b), Electrodynamics in a rotating frame of reference with application to global ocean circulation, *Can. J. Phys.*, *73*, 393–402.

Tyler, R. H., S. Maus, and H. Lühr (2003), Satellite observations of magnetic fields due to ocean tidal flow, *Science*, *299*, 239–241.

Tyler, R. H., F. Vivier, and S. Li (2004), Three-dimensional modelling of ocean electrodynamics using gauged potentials, *Geophys. J. Int.*, *158*, 874–887.

Vivier, F., E. Maier-Reimer, and R. H. Tyler (2004), Simulations of magnetic fields generated by the Antarctic Circumpolar Current at satellite altitude: Can geomagnetic measurements be used to monitor the flow?, *Geophys. Res. Lett.*, *31*, L10306, doi:10.1029/2004GL019804.

Z. B. Szuts, Max-Planck-Institut für Meterologie, Bundesstr. 53, D-20146 Hamburg, Germany. (zoltan.szuts@zmaw.de)